대한영상의학회지

Adaptive Image Rescaling for Weakly Contrast-Enhanced Lesions in Dedicated Breast CT: A Phantom Study

약하게 조영증강된 병변의 유방 전용 CT 영상의 대조도 개선을 위한 적응적 영상 재조정 방법: 팬텀 연구

*Corresponding author
Hosang Jeon, PhD
Department of Radiation
Oncology and Research Institute
for Convergence of Biomedical
Science and Technology,
Pusan National University
Yangsan Hospital,
20 Geumo-ro, Mulgeum-eup,
Yangsan 50612, Korea.

Tel 82-55-360-3458
Fax 82-55-360-3449
E-mail hjeon316@gmail.com

Bitbyeol Kim, MS[1] , Ho Kyung Kim, PhD[1] , Jinsung Kim, PhD[2] ,
Yongkan Ki, MD[3] , Ji Hyeon Joo, MD[4] , Hosang Jeon, PhD[4]* ,
Dahl Park, PhD[5] , Wontaek Kim, MD[3] ,
Jiho Nam, MD[5] , Dong Hyeon Kim, MD[5]

[1]School of Mechanical Engineering and the Center for Advanced Medical Engineering Research, Pusan National University, Busan, Korea
[2]Department of Radiation Oncology, Yonsei Cancer Center, Yonsei University College of Medicine, Seoul, Korea
[3]Department of Radiation Oncology, Pusan National University School of Medicine, Yangsan, Korea
[4]Department of Radiation Oncology and Research Institute for Convergence of Biomedical Science and Technology, Pusan National University Yangsan Hospital, Yangsan, Korea
[5]Department of Radiation Oncology, Pusan National University Hospital, Busan, Korea

ORCID iDs
Bitbyeol Kim
https://orcid.org/0000-0002-2204-6144
Ho Kyung Kim
https://orcid.org/0000-0003-1261-6411
Jinsung Kim
https://orcid.org/0000-0003-1415-6471
Yongkan Ki
https://orcid.org/0000-0003-0757-8211
Ji Hyeon Joo
https://orcid.org/0000-0001-9275-3197
Hosang Jeon
https://orcid.org/0000-0003-3960-3469
Dahl Park
https://orcid.org/0000-0001-5143-3920
Wontaek Kim
https://orcid.org/0000-0001-8626-7344
Jiho Nam
https://orcid.org/0000-0001-8495-0166
Dong Hyeon Kim
https://orcid.org/0000-0002-8062-4619

Purpose Dedicated breast CT is an emerging volumetric X-ray imaging modality for diagnosis that does not require any painful breast compression. To improve the detection rate of weakly enhanced lesions, an adaptive image rescaling (AIR) technique was proposed.

Materials and Methods Two disks containing five identical holes and five holes of different diameters were scanned using 60/100 kVp to obtain single-energy CT (SECT), dual-energy CT (DECT), and AIR images. A piece of pork was also scanned as a subclinical trial. The image quality was evaluated using image contrast and contrast-to-noise ratio (CNR). The difference of imaging performances was confirmed using student's *t* test.

Results Total mean image contrast of AIR (0.70) reached 74.5% of that of DECT (0.94) and was higher than that of SECT (0.22) by 318.2%. Total mean CNR of AIR (5.08) was 35.5% of that of SECT (14.30) and was higher than that of DECT (2.28) by 222.8%. A similar trend was observed in the subclinical study.

Conclusion The results demonstrated superior image contrast of AIR over SECT, and its higher overall image quality compared to DECT with half the exposure. Therefore, AIR seems to have the potential to improve the detectability of lesions with dedicated breast CT.

Index terms Breast Cancer; Computed Tomography, X-Ray; Contrast Agent; Image Quality Enhancement

INTRODUCTION

Breast cancer is one of the most frequently occurring cancers and the leading cause of death from cancer among women worldwide (1). However, despite the increase in the number of breast cancer cases in recent years, mortality from breast cancer has shown a declining trend (2). Early detection and subsequent treatment of breast cancer may explain this conflicting trend. Since the breast cancer is mainly begun within breast parenchyma such as the ducts (the pipeline for the flow of milk) or the lobules (the breast gland at the terminal of duct network), the diagnostic imaging of breast has been an effective modality for breast cancer screening (3). Currently, mammography and digital breast tomosynthesis (DBT) are the standard imaging modalities for breast cancer screening, and advanced imaging technologies such as contrast-enhanced MRI have also been used to diagnose breast cancer (4).

Dedicated breast CT (BCT) has recently been used as a new three-dimensional (3D) diagnostic imaging system that can improve the early detection of breast cancer (5, 6). It can provide 3D anatomical information with higher detectability of imaging targets, especially malignant tumors in dense breasts, than conventional two-dimensional (2D) mammography or DBT, which have the drawback of superimposition of anatomies (7-9). Moreover, according to a review paper (7) that evaluated the studies on BCT carried out since 2001, BCT can produce breast images using a patient exposure comparable to that of conventional two-view mammography in spite of higher dose than simple 2D imaging. In addition, BCT can avoid the painful physical compression of patients' breasts, which is essential for mammography and DBT. Lindfors et al. (5) reported that there was no meaningful difference between BCT and mammography in distinguishing malignant and benign tumors in a preliminary clinical study in 2008.

Meanwhile, the usefulness of contrast-enhanced imaging in distinguishing benign and malignant tissues has been demonstrated by several researchers (10-13). In BCT, contrast-enhanced images showed considerable differential enhancement between malignant (55.9 ± 4.0 Hounsfield unit [HU]) and benign (17.6 ± 6.1 HU) images, which was superior to that of unenhanced images (14). However, it is possible that small or weakly contrast-enhanced lesions may not be detected, but these may be an important sign of early breast cancer. In the clinical field, dual-energy CT (DECT) is generally used to increase the detectability of contrast-enhanced lesions using a material decomposition technique, which was first introduced in the 1970s (15-17). DECT can provide an outstanding image contrast by combining two different X-ray energetic CT images compared to single-energy CT (SECT). It utilizes lower and higher tube voltages, which are chosen so that the K-edge of the iodine lies between their mean energies, thus enabling differentiation of iodine-enhanced lesions from other materials (18, 19).

However, DECT generally requires double scans and/or double exposure of the patient in principle, and the X-ray energy level used for DECT may be too high to scan small objects such as breasts optimally. In addition, if double scans are applied, the relatively long scan time may cause image artifacts to be generated by the patient's motion.

We proposed an adaptive image rescaling (AIR) method suitable for dedicated BCT to clarify small or weakly contrast-enhanced lesions. It requires only a single scan and subsequent X-ray penetration length estimation to enhance the target material. This concept was first intro-

duced by Kis et al. (20) through the distinguishment of bone and soft tissues of a virtual phantom using a computer simulation. They also showed that the single-scan and length estimation method demonstrated an imaging performance similar to that of the dual-scan variant. In this study, we experimentally assessed the feasibility of the AIR method for high detectability of small or weakly iodinated lesions by objectively calculating an optimal rescaling threshold.

MATERIALS AND METHODS

THEORY

A cone-beam CT system consisting of a kilo-voltage X-ray generator and a flat-panel detector is generally adopted for dedicated BCT; therefore, we designed AIR algorithm suitable for the system. The projection image acquired by the flat-panel detector is a distribution of the mean attenuation coefficients of voxels lying on the corresponding X-ray beam path length $L(x)$ penetrating an imaging object, where x denotes the 2D coordinate vector of the projection image. We used the ray-tracing method proposed by Siddon (21) to compute the X-ray path lengths from the reconstructed image:

$$L(x) = \sum l(u; x) \qquad\qquad 1)$$

where l is the path length within a single voxel along the corresponding penetration path, and u is the 3D coordinate vector of the reconstructed volume. A conceptual description of the X-ray penetration path length estimation is shown in Fig. 1.

Assuming that an imaging object consists of two materials, tissue and contrast agent, a sinogram p can be expressed using the first-order approximation of Beer's law (22):

$$p(x) = -\ln \frac{I(x)}{I_0(x)} = \mu_c \cdot L_c(x) + \mu_t \cdot L_t(x) \qquad\qquad 2)$$

where I and I_0 are the signal intensities with and without the imaging object, respectively,

Fig. 1. Conceptual description of the X-ray penetration path length in cone-beam CT.
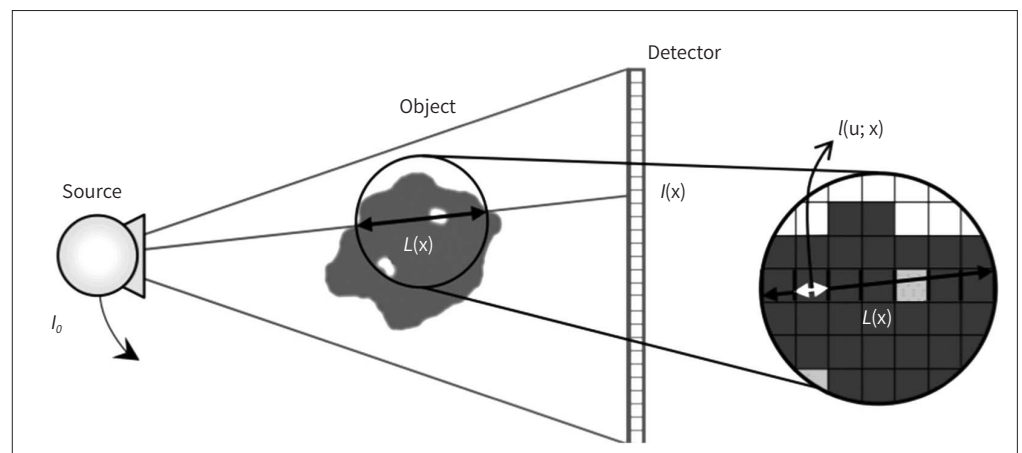
and μ_c and μ_t are the mean attenuation coefficients of the contrast agent and tissue, respectively. L_c and L_t represent the subtotal penetration path lengths of the contrast agent and tissue, respectively. The total penetration path length $L(x)$ is the sum of L_c and L_t, expressed as:

$$L(x) = L_c(x) + L_t(x) \qquad\qquad 3)$$

$L(x)$ can be computed from the reconstructed image. First, the boundary of the imaging object was identified using an adaptive thresholding method, and we assigned unity to the inside of the object and zero to the rest. Second, the $L(x)$ values in all x positions were acquired through forward projection of the binary image according to Eq.1. Third, the $L_c(x)$ and $L_t(x)$ values were obtained by solving Eq.2 and Eq.3 simultaneously. A scheme for this AIR algorithm is illustrated in Fig. 2. The final output of AIR is in the form of a material-selective image that can be reconstructed from either $L_c(x)$ or $L_t(x)$ given in the form of a sinogram.

For the comparison of imaging performances, we reconstructed DECT images using a conventional image-based material decomposition algorithm (i.e., image blending), which is a widely-used dual-energy data-processing method (23, 24). The reconstructed CT image data using low and high tube voltages can be expressed as follows:

$$\mu_{eff,L}(u) = m_c \cdot \mu_{c,L}(u) + m_t \cdot \mu_{t,L}(u) \qquad\qquad 4)$$
$$\mu_{eff,H}(u) = m_c \cdot \mu_{c,H}(u) + m_t \cdot \mu_{t,H}(u) \qquad\qquad 5)$$

where $\mu_{eff,L}$ and $\mu_{eff,H}$ denote the CT voxel values (or effective attenuation coefficients) using the low and high tube voltages, respectively, and m is the mass fraction. We measured four μ values of iodine contrast and tissue-equivalent polymethyl-methacrylate (PMMA), i.e., $\mu_{c,L}$, $\mu_{t,L}$, $\mu_{c,H}$, and $\mu_{t,H}$, using a dedicated PMMA disk phantom with a hole filled with the iodine contrast. By solving Eq.4 and Eq.5 simultaneously, we obtained an m_c-distribution and an m_t-distribution, representing a contrast-selective image and a tissue-selective image, respective-

Fig. 2. Scheme of the adaptive image rescaling algorithm (A-F).
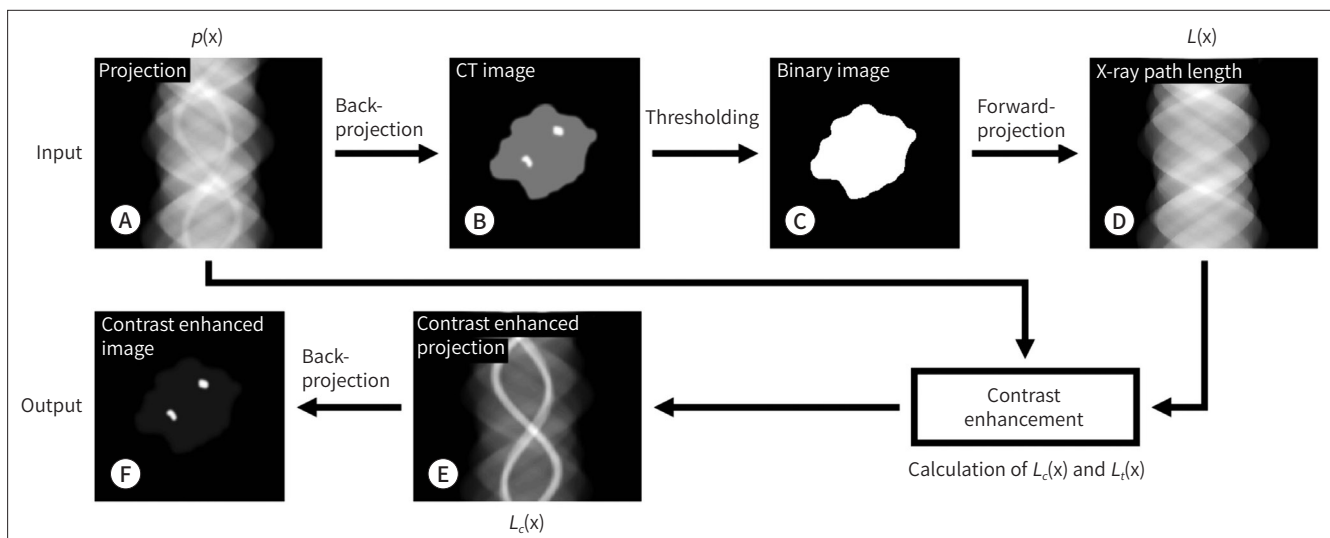
ly. A correlated noise reduction algorithm suggested by Kalender et al. (25) was adopted to reduce the increased stochastic noise through the material decomposition process of DECT (26).

EXPERIMENTAL CONDITIONS

Two disk phantoms, each with a diameter of 70 mm, were manufactured using PMMA material for the performance evaluation of material decomposition. Disk A had five holes of equal diameter (5 mm), which were filled with iodine contrast agents of various concentrations of 5, 10, 20, 40, and 80 mg/mL to cover the range actually used in human body. Disk B had five holes with various diameters of 1, 2, 3, 4, and 5 mm to mimic contrast-enhanced lesions of various small sizes. All holes were filled with iodine contrast agent with the same concentration of 20 mg/mL, which was the median value of all concentrations in disk A. The details of the disk phantoms are illustrated in Fig. 3.

As shown in Fig. 4, a benchtop CT system composed of an X-ray tube (E7239X, Toshiba, Tokyo, Japan) with a tungsten anode and a flat-panel detector (Shad-o-Box HS, Dalsa, Waterloo, Canada) was used to scan the disk phantom. The pitch of the detector pixel was 0.099 mm, and the magnification ratio was 1.78. The inherent filtration of the tube was 0.7 mm Al equivalent at 62.5 kV, and the X-ray field size was 354×354 mm^2 at a distance of 750 mm. The source-to-detector distance was 1420 mm and the source-to-axis distance was 800 mm.

For CT image reconstruction, the Feldkamp–Davis–Kress algorithm (27), which is an extended 3D approximation of the 2D filtered back-projection algorithm of conventional fan-beam CT imaging, was employed. All reconstructed volumes consisted of $750 \times 750 \times 500$ voxels with a one-side length of 0.12 mm. We measured the projection images at 60 kVp to reconstruct SECT images, which were also used as inputs to the AIR algorithm. Reconstructed images at 100 kVp were obtained for DECT. All CT images were reconstructed with Wiener filtration for reducing the noise, and the uniformity was evaluated to 2.9% as the standard deviation of a reconstructed flood image. We maintained the imaging dose of approximately 2 mGy per rotation to evaluate the performance of AIR at low dose levels. A solid-state X-ray dosimeter (Piranha 657, RTI, Mölndal, Sweden) was placed at the isocenter of our CT system

Fig. 3. Details of the disk phantoms made of PMMA with five holes filled with iodinated contrast agent.
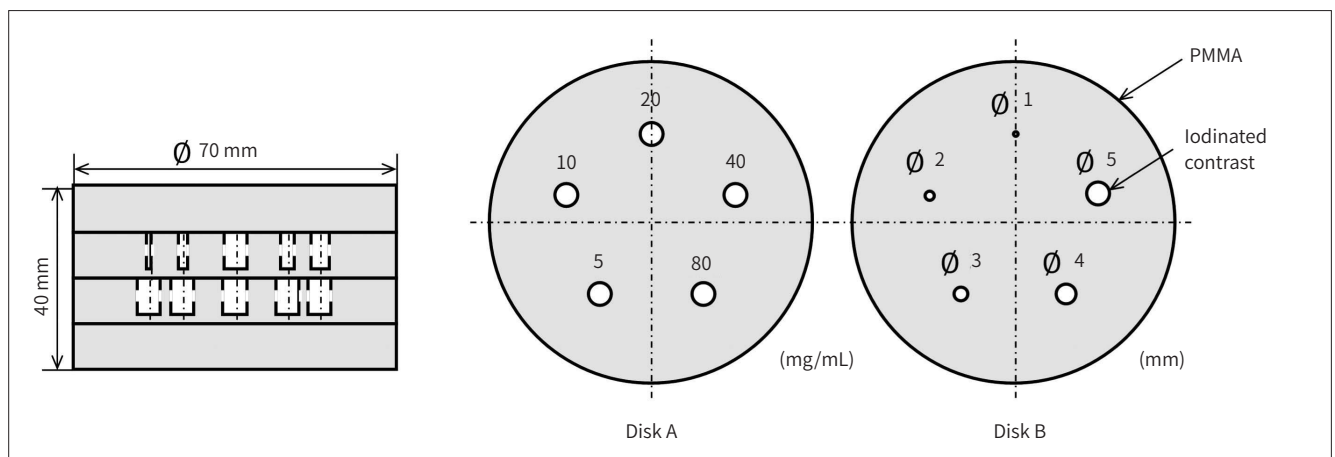
PMMA = polymethyl-methacrylate

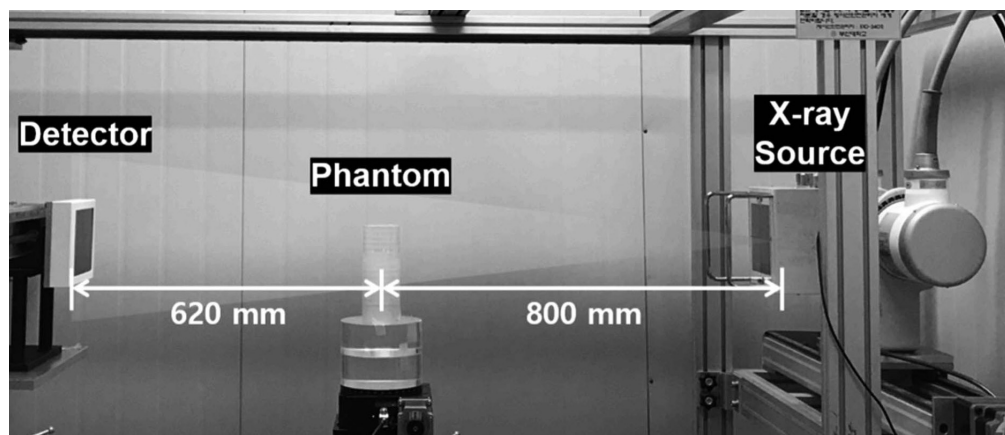**Fig. 4.** Experimental setup of a benchtop CT imaging system.

Table 1. Information on Imaging Exposures with Low and High X-Ray Energies

Energy	Tube			Air Kerma (Measured)	
	Voltage (kVp)	Current (mA)	Time (ms)	1 Projection (Gy)	360 Projections (mGy)
Low	60	40	8	6.84	2.46
High	100	10	10	6.28	2.26

to measure air kerma to acquire a projection image. To mimic the environment at the center of the disk phantom, we placed a PMMA block with a thickness of 35 mm, the radius of the phantom, in front of the dosimeter toward the tube. In this study, 360 projection images taken at every one-degree angle were used to reconstruct a CT image set. The measured air kerma data and relevant X-ray beam conditions are summarized in Table 1. The total exposure of DECT is equal to the sum of the exposures of the 60 kVp and 100 kVp scans, and the exposure required for AIR is equal to that of the 60 kVp scan.

IMAGE ANALYSIS

We assessed the image contrast of iodinated regions of interest (ROIs) in the phantom because their conspicuity was essential to achieve a higher detection rate. The contrast-to-noise ratio (CNR) was also used to address the effect of image noise on conspicuity. The image contrast and CNR were calculated as follows:

$$\text{Image contrast} = \frac{|I_{ROI}\text{-}I_{bgn}|}{I_{ROI}+I_{bgn}}, \quad \text{CNR} = \frac{|I_{ROI}\text{-}I_{bgn}|}{\sigma_{ROI}^2+\sigma_{bgn}^2} \qquad 6)$$

where I_{ROI} and I_{bgn} denote the mean CT numbers of the ROI and neighboring background, respectively, and σ refers to their standard deviations. The ROI and background region were square and their sizes were fixed at 20 × 20 pixels, except for the ROIs of disk B, which were proportional to hole sizes. We selected 15 backgrounds to consider the possible variations in image contrast and CNR; thus, 15 image contrast and CNR values were obtained for each image. The image contrast and CNR of AIR were statistically compared to those of SECT and DECT, respectively, using student's t test. Additionally, in the case of disk A, the relevance of CT number to iodine concentration was also evaluated.

SUBCLINICAL STUDY

To evaluate the imaging performance in a tissue-equivalent environment, we used a piece of pork with five holes of similar diameters of approximately 3 mm. Three holes were filled with iodinated contrast as a concentration of 10 mg/mL to simulate weakly-enhanced lesions, and the rest with contrast at a concentration of 20 mg/mL. The image contrast and CNR were assessed in the same manner as in the disk phantom.

RESULTS

IODINE CONCENTRATION

We acquired a reconstructed image of disk A including five holes filled with different concentrations of iodinated contrast and subsequently extracted an AIR-processed image from it. A DECT image was also acquired using the two reconstructed images at 60 and 100 kVp. All reconstructed images are presented in Fig. 5.

As presented in Table 2, the mean image contrast of AIR (0.67) reached 71.6% of that of DECT (0.93), and apart from the lowest two concentrations, image contrast values of AIR

Fig. 5. Three reconstructed images of disk A (transverse view).
A-C. Single-energy CT (A), dual-energy CT (B), and adaptive image rescaling (C) images for disk A. All images were normalized to unity at region of interest of 20 mg/mL, and window width is [0 1].
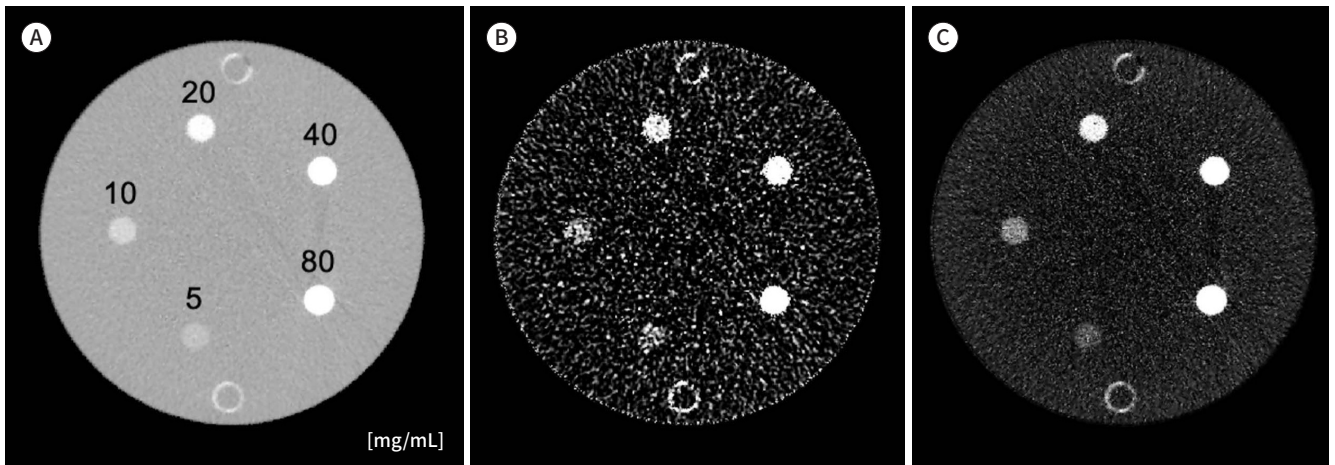

Table 2. Image Contrast and CNR Values with Respect to Iodine Concentrations in Disk A

Concentration (mg/mL)	Image Contrast			CNR		
	SECT	DECT	AIR	SECT	DECT	AIR
5	0.06 ($p < 0.001$)	0.88 ($p < 0.001$)	0.37 (-)	3.42 ($p < 0.001$)	1.04 ($p < 0.001$)	1.15 (-)
10	0.11 ($p < 0.001$)	0.90 ($p < 0.001$)	0.56 (-)	7.42 ($p < 0.001$)	1.21 ($p < 0.001$)	2.24 (-)
20	0.20 ($p < 0.001$)	0.94 ($p = 0.002$)	0.70 (-)	13.10 ($p < 0.001$)	2.08 ($p < 0.001$)	4.35 (-)
40	0.33 ($p < 0.001$)	0.96 ($p = 0.007$)	0.82 (-)	26.86 ($p < 0.001$)	3.40 ($p = 0.007$)	8.74 (-)
80	0.49 ($p < 0.001$)	0.98 ($p = 0.021$)	0.90 (-)	37.09 ($p < 0.001$)	5.16 ($p = 0.023$)	14.27 (-)
Mean	0.24	0.93	0.67	17.58	2.58	6.15

All p values were calculated using student's t test with AIR.
AIR = adaptive image rescaling, CNR = contrast-to-noise ratio, DECT = dual-energy CT, SECT = single-energy CT

were more than 84% of those of DECT. At the lowest and highest concentrations, image contrast values of AIR were 42.4 ± 25.7% and 92.5 ± 3.3% of those of DECT, respectively. The mean image contrast of AIR (0.67) was much higher than that of SECT (0.24) by 279%.

In the case of CNR, AIR presented a moderate performance between those of SECT and DECT, as presented in Table 2. The mean CNR of AIR (6.15) was 35.0% of that of SECT (17.58), and a similar percentage difference in CNR was shown between SECT and AIR at all concentrations of iodine, unlike in the case of contrast values. Meanwhile, the mean CNR of AIR (6.15) was superior to that of DECT (2.58) by 238.4%. However, this superiority of AIR decreased as the concentration of iodine decreased. All measured image contrast and CNR values for disk A are summarized in Table 2, and plotted in Fig. 6. All p values of student's t test were lower than 0.05.

To verify the linearity between image pixel intensity and iodine concentration, we plotted their relationships with the normalization to unity at 5 mg/mL, as shown in Fig. 7. The slope

Fig. 6. Comparison of imaging performances using disk A.
A, B. Contrast (A) and CNR (B) curves with respect to the iodine concentrations in disk A.
AIR = adaptive image rescaling, CNR = contrast-to-noise ratio, DECT = dual-energy CT, SECT = single-energy CT
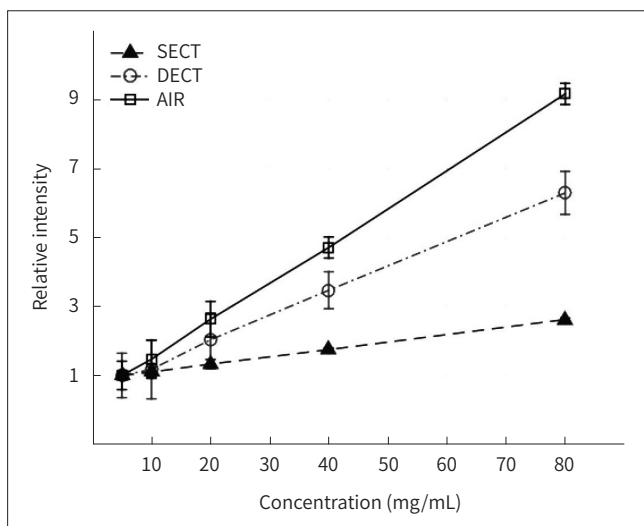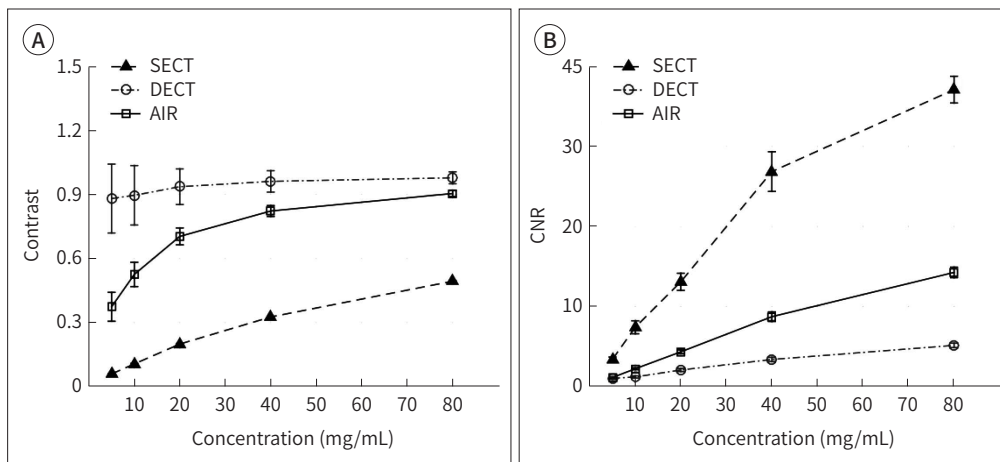

Fig. 7. Linearity between image intensities and iodine concentration for SECT, DECT, and AIR.
AIR = adaptive image rescaling, DECT = dual-energy CT, SECT = single-energy CT

gradients, representing the increase in image pixel intensity per unit concentration, were 0.022, 0.070, and 0.109 for SECT, DECT, and AIR, respectively, and the Pearson coefficients of them were higher than 0.999.

SPATIAL RESOLUTION

We acquired a reconstructed SECT image of disk B, which had five holes of different diameters filled with the same concentration of iodinated contrast, 20 mg/mL. The AIR-processed and DECT images were acquired in the same manner as in the case of disk A. All reconstructed images are shown in Fig. 8.

The contrast values of different ROIs appear to be constant in all images. AIR presented a moderate image contrast between those of SECT and DECT as presented in Table 3, and the mean image contrast of AIR (0.73) was 77.7% of that of DECT (0.94). The mean contrast value of AIR (0.73) was 365.0% higher than that of SECT (0.20).

The CNR values of different ROIs appear similar within a certain range in all images, except for the smallest ROI with a diameter of 1 mm, as shown in Fig. 9B. The mean CNR of

Fig. 8. Three reconstructed images of disk B (transverse view).
A-C. Single-energy CT (A), dual-energy CT (B), and adaptive image rescaling (C) images for disk B. All images were normalized to 1 at region of interest of 5 mm, and window width is [0 1].
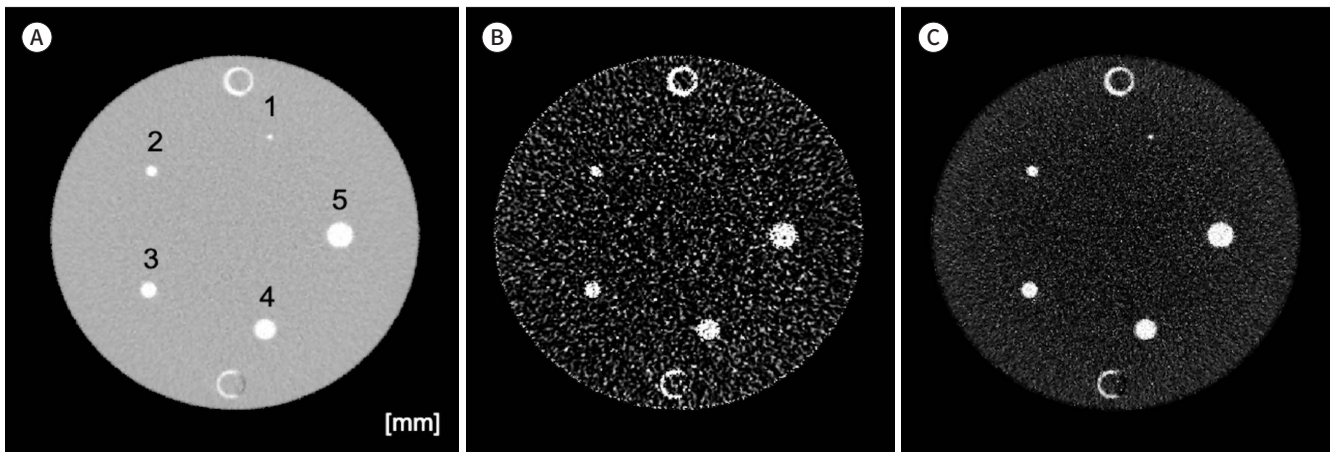

Table 3. Image Contrast and CNR Values with Respect to the Size of ROIs in Disk B

Diameter (mm)	Image Contrast			CNR		
	SECT	DECT	AIR	SECT	DECT	AIR
1	0.19 ($p < 0.001$)	0.96 ($p = 0.304$*)	0.72 (-)	4.72 ($p < 0.001$)	1.49 ($p = 0.889$*)	2.53 (-)
2	0.20 ($p < 0.001$)	0.94 ($p < 0.001$)	0.73 (-)	12.18 ($p < 0.001$)	2.37 ($p < 0.001$)	4.49 (-)
3	0.21 ($p < 0.001$)	0.94 ($p < 0.001$)	0.74 (-)	12.56 ($p < 0.001$)	2.06 ($p < 0.001$)	4.17 (-)
4	0.21 ($p < 0.001$)	0.94 ($p < 0.001$)	0.74 (-)	13.17 ($p < 0.001$)	2.00 ($p < 0.001$)	4.48 (-)
5	0.20 ($p < 0.001$)	0.94 ($p = 0.002$)	0.74 (-)	12.45 ($p < 0.001$)	1.92 ($p = 0.003$)	4.33 (-)
Mean	0.20	0.94	0.73	11.02	1.97	4.00

All p values were calculated using student's t test with AIR.
*Indicate p values greater than 0.05.
AIR = adaptive image rescaling, CNR = contrast-to-noise ratio, DECT = dual-energy CT, ROI = region of interest, SECT = single-energy CT

Fig. 9. Comparison of imaging performances using disk B.
A, B. Contrast (A) and CNR (B) curves with respect to the diameters of regions of interest in disk B.
AIR = adaptive image rescaling, CNR = contrast-to-noise ratio, DECT = dual-energy CT, SECT = single-energy CT
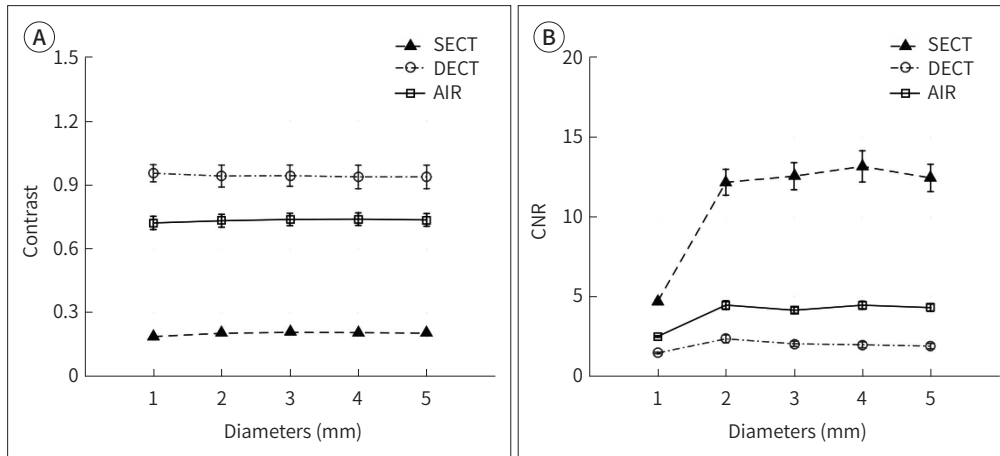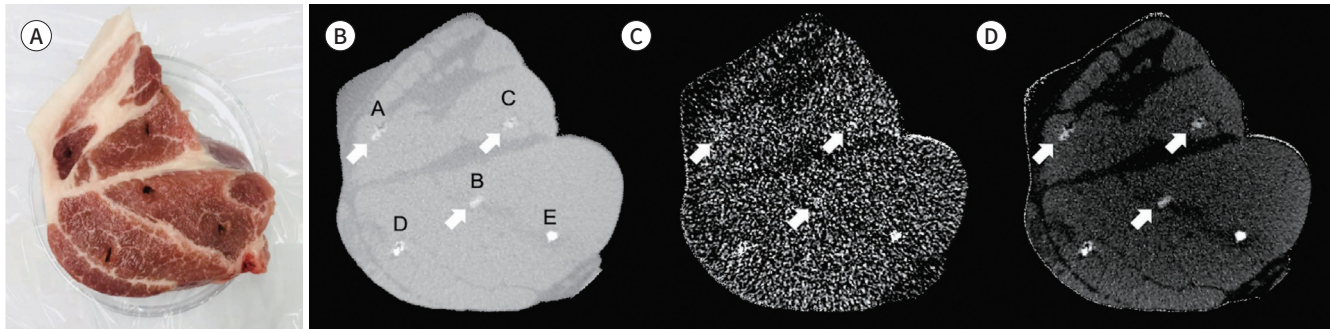

Fig. 10. Comparison of imaging performances in a subclinical trial.
A-D. Single-energy CT (B), dual-energy CT (C), and adaptive image rescaling (D) images of a piece of pork (A) with five iodine inserts in the subclinical study (A, B, C: 10 mg/mL; D, E: 20 mg/mL).


AIR (4.00) was 202.8% of that of DECT (1.97), and the CNR difference between them decreased as the diameter of the ROI decreased. At the smallest ROI, SECT showed a significantly lower CNR value than at other ROIs, owing to the high fluctuation of image intensities inside the ROI. All measured contrast and CNR data are summarized in Table 3. All *p* values of student's *t* test were lower than 0.05, except for the ROI with diameter of 1 mm of DECT.

SUBCLINICAL STUDY

All reconstructed images of a piece of pork with five holes were acquired under the same experimental conditions as for the disk phantom as shown in Fig. 10. In most images, the contrast values were comparably consistent with those of the corresponding disk phantom images. However, mean CNR ratios of the subclinical images to disk A images of SECT, DECT, and AIR were 16.8, 39.8, and 61.2% at 10 mg/mL, respectively. In case of 20 mg/mL, they were 14.3, 34.5, and 31.0%, respectively. The quantitative results are presented in Fig. 11; we found that the contrast of AIR was comparable to that of DECT, and that the CNR of AIR was comparable to that of SECT.

Fig. 11. Comparison of the contrast and CNR values between SECT, DECT, and AIR.
AIR = adaptive image rescaling, CNR = contrast-to-noise ratio, DECT = dual-energy CT, SECT = single-energy CT
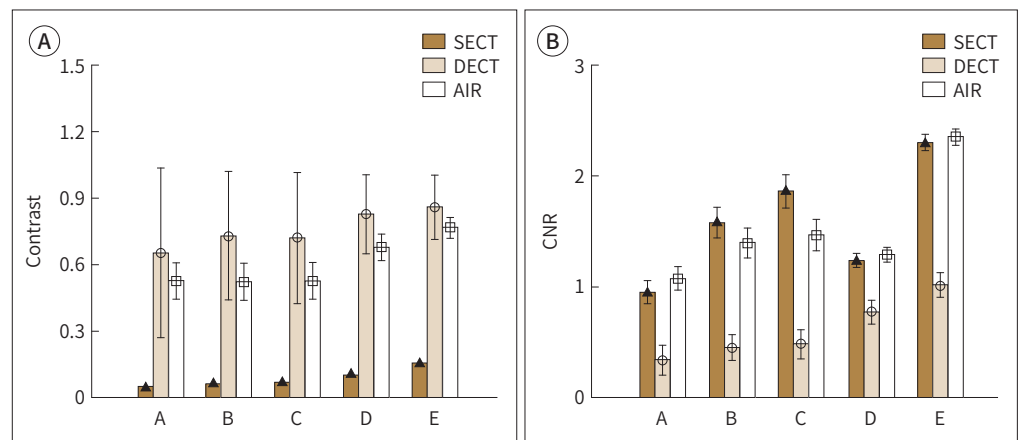

DISCUSSION

The improved conspicuity of target lesions through material decomposition with the dual-energy imaging technique comes at the cost of increased stochastic image noise due to the combination or addition of the inherent stochastic noise of two different CT image sets. However, solving Eq.4 and Eq.5 is intrinsically a subtractive process that causes a reduction in signal size, which means that the signal-to-noise ratio can be significantly reduced. Thus, noise reduction strategies are often employed for the dual-energy technique to suppress image noise (25, 26, 28-30). The AIR method introduced in this study uses a single CT image set and X-ray penetration length information computed from it, as described in Fig. 2. Because the noise component of the image set partially disappears owing to the binarization process during the estimation of the penetration lengths, the resultant image generated by AIR is affected by the noise of the original image set itself. Finally, the images post-processed by AIR presented good image contrasts comparable to DECT and showed moderate CNRs between those of SECT and DECT, as presented in Figs. 6 and 9, respectively. Because the quality of image noise in AIR was superior to that in DECT, the CNR of AIR was higher than that of DECT. It was also statistically confirmed that the performance of AIR showed a significant difference compared to that of SECT or DECT using student's t test as shown in Tables 2 and 3.

Although the image contrast of DECT is superior to that of AIR, the relatively high noise levels made it more difficult to maintain superiority in the conspicuity of ROIs. For example, considering p values greater than 0.05, DECT was not superior to AIR in case of ROI with diameter of 1 mm in disk B as shown in Table 3. Considering the significant influence of noise on the visual reading of diagnostic images, the low-noise characteristic of AIR can be an important feature that enables AIR to be theoretically comparable to conventional DECT. A comparison of the central line profiles of the ROI with a diameter of 3 mm (Fig. 12) could support this point. Nevertheless, further studies should be conducted to make actual noise comparisons between DECT and AIR, because a variety of advanced noise reduction algorithms have been adopted for commercial DECT systems.

Fig. 12. Comparison of central line profiles of the 3 mm-diameter region of interest in single-energy CT (A), dual-energy CT (B), and adaptive image rescaling (C). Each curve was normalized to 1 at its own maximum intensity.
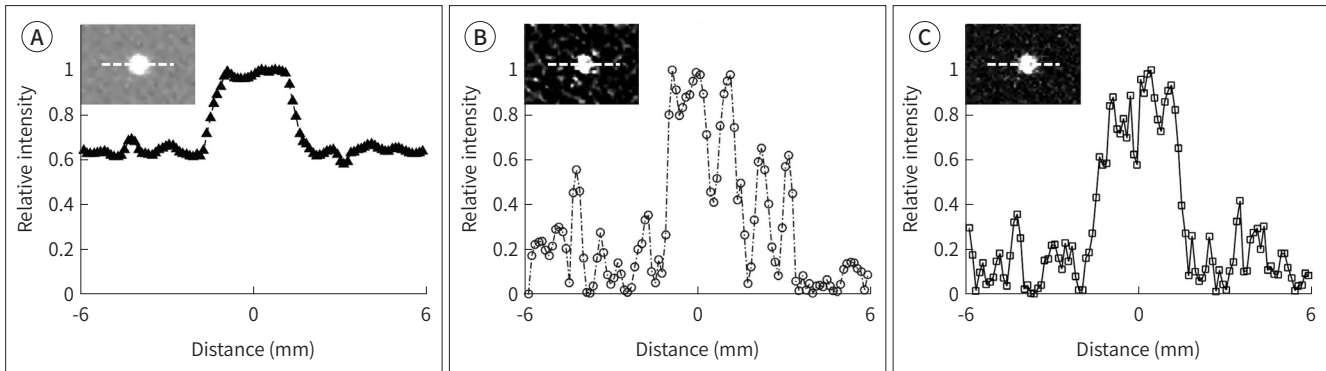
A single scan is obviously preferred over a dual scan in terms of patient exposure and scanning time. An equivalent dose is generally required to obtain each image set in the dual scan of DECT; however, AIR requires roughly half of the total dose while providing a comparable image quality as mentioned above. Moreover, we demonstrated that AIR showed a low image noise characteristic despite relatively low imaging doses (approximately 2 mGy per scan). The typical imaging doses used for 2D mammography and 3D abdominal CT are 3 mGy and 10 mGy, respectively, and the potential cancer risk caused by a diagnostic CT imaging dose has already been reviewed by Brenner and Hall (31). The scanning time of AIR, which is approximately half that of DECT, can also improve the convenience to the patient and minimize motion artifacts.

As mentioned above, only one image set using a single tube voltage was required to implement the AIR algorithm. Considering the K-edge of iodine (33 keV), it is strongly recommended for one of the two different tube voltages essential to conventional DECT to be more than 100 kVp. However, such a high tube voltage has not been preferred in dedicated BCT studies. Several researchers have mentioned that a tube voltage in the range of 60–80 kVp is suitable for obtaining a uniform dose distribution and good image quality for BCT (9, 32, 33). The AIR method is theoretically less dependent on the tube voltage, and we obtained remarkable results using 60 kVp as shown in the previous section. This implies that the AIR algorithm can be applied to existing BCT systems without any additional hardware cost.

In the subclinical study, as plotted in Fig. 11, the image produced using AIR presented a similar imaging performance to that in the disk phantom study. Because noise components of holes A and D were overestimated owing to their irregular shapes as shown in Fig. 10B, CNR values of them were relatively low compared to others with same iodine concentrations. The image contrast of AIR was comparable to that of DECT, and the overall increase in image noise appeared to have slightly increased the CNR difference between AIR and DECT. Therefore, AIR is expected to show the usable imaging performance, especially at lower concentrations of contrast material (see arrows in Fig. 10), which might be clinically important for increasing the detection rate. Although the contrast and CNR of AIR in the subclinical study were lower than those of the disk phantom images owing to the inhomogeneity in biological tissues, we noted that this subclinical study demonstrated high feasibility for the clinical ap-

plication of AIR because the rescaled image that was adaptively optimized for the individual case could be acquired.

The AIR algorithm has some limitations. First, the X-ray penetration lengths should be carefully estimated to achieve accurate results. For example, if the original SECT image is defectively reconstructed owing to metal or motion artifacts, it becomes difficult to identify the actual body surface, which may cause an additional noise component in the resultant images. In the breast, fortunately, prostheses causing metal artifacts are rare. However, the respiration of patients should be properly controlled. In addition, the scanning field of view of CT should cover the whole breast because the truncation of projection images may cause imaging artifacts.

Second, the performance of AIR is dependent on the attenuation coefficient μ. In fact, the main issue in the field of material decomposition is also to find the effective μ values of basic materials, which are difficult to accurately compute owing to the poly-energetic and scatter characteristics of X-rays. Thus, some researchers have introduced empirical calibration techniques to avoid these difficulties (34-37). In this study, we directly measured μ_c and μ_t using a dedicated disk phantom with a hole filled by an iodinated contrast material with a known iodine concentration. Considering the tissue homogeneity in the anatomy of the breast, the measured μ values from the phantom were expected to be applicable in clinical situations, although the image quality in our subclinical study was slightly lower than that in the phantom study. We intend to conduct further research to improve the overall image quality of AIR by implementing hardware configurations and noise reduction algorithms optimized to more clinical objects such as cadaveric breasts and finding more effective μ values of the basic materials through a calibration procedure suitable to dedicated BCT systems. The phantom containing three or more different materials that mimic artificial inserts such as breast expanders will be also studied to evaluate the practical use of AIR in clinical situation. In addition, the analysis of performance evaluation metrics, such as sensitivity and specificity, using a number of subclinical or clinical images will be included in our further study to verify the performance of AIR.

In conclusion, the performance of AIR method was verified to provide the superior image contrast over SECT and the higher CNR compared to DECT with half the exposure. Therefore, AIR is expected to show the potential to improve the detectability of lesions for dedicated breast CT.

Author Contributions

Conceptualization, K.H.K., K.J.; data curation, N.J.; formal analysis, K.Y., N.J.; funding accquistion, K.J.; investigation, K.B., J.J.H.; methodology, K.B.; project administration, K.H.K; resources, K.Y., K.W.; software, K.B.; supervision, J.J.H.; validation, P.D., K.W.; visualization, K.B., K.D.H.; writing—original draft, K.B., J.H.; and writing—review & editing, J.H., K.H.K.

Conflicts of Interest

The authors have no potential conflicts of interest to disclose.

Funding

REFERENCES

1. International Agency for research on Cancer. *WHO GLOBOCAN cancer facts sheets: breast cancer.* Lyon: WHO 2012
2. Torre L, Siegel R, Jemal A. *Global cancer facts & figures.* 3rd ed. Atlanta: American Cancer Society 2015
3. Kopans DB. *Breast imaging.* 3rd ed. Philadelphia: Lippincott Williams & Wilkins 2007
4. Karellas A, Vedantham S. Breast cancer imaging: a perspective for the next decade. *Med Phys* 2008;35:4878-4897
5. Lindfors KK, Boone JM, Nelson TR, Yang K, Kwan AL, Miller DF. Dedicated breast CT: initial clinical experience. *Radiology* 2008;246:725-733
6. Yang WT, Carkaci S, Chen L, Lai CJ, Sahin A, Whitman GJ, et al. Dedicated cone-beam breast CT: feasibility study with surgical mastectomy specimens. *AJR Am J Roentgenol* 2007;189:1312-1315
7. Sarno A, Mettivier G, Russo P. Dedicated breast computed tomography: basic aspects. *Med Phys* 2015;42:2786-2804
8. O'Connell AM, Karellas A, Vedantham S. The potential role of dedicated 3D breast CT as a diagnostic tool: review and early clinical examples. *Breast J* 2014;20:592-605
9. Boone JM, Nelson TR, Lindfors KK, Seibert JA. Dedicated breast CT: radiation dose and image quality evaluation. *Radiology* 2001;221:657-667
10. Goh V, Padhani AR. Imaging tumor angiogenesis: functional assessment using MDCT or MRI? *Abdom Imaging* 2006;31:194-199
11. Dawson P. Functional imaging in CT. *Eur J Radiol* 2006;60:331-340
12. Miles KA. Tumour angiogenesis and its relation to contrast enhancement on computed tomography: a review. *Eur J Radiol* 1999;30:198-205
13. Cuenod CA, Fournier L, Balvay D, Guinebretière JM. Tumor angiogenesis: pathophysiology and implications for contrast-enhanced MRI and CT assessment. *Abdom Imaging* 2006;31:188-193
14. Prionas ND, Lindfors KK, Ray S, Huang SY, Beckett LA, Monsky WL, et al. Contrast-enhanced dedicated breast CT: initial clinical experience. *Radiology* 2010;256:714-723
15. Millner MR, McDavid WD, Waggener RG, Dennis MJ, Payne WH, Sank VJ. Extraction of information from CT scans at different energies. *Med Phys* 1979;6:70-71
16. Avrin DE, Macovski A, Zatz LE. Clinical application of Compton and photo-electric reconstruction in computed tomography: preliminary results. *Invest Radiol* 1978;13:217-222
17. Chiro GD, Brooks RA, Kessler RM, Johnston GS, Jones AE, Herdt JR, et al. Tissue signatures with dual-energy computed tomography. *Radiology* 1979;131:521-523
18. Riederer SJ, Mistretta CA. Selective iodine imaging using K-edge energies in computerized x-ray tomography. *Med Phys* 1977;4:474-481
19. Coursey CA, Nelson RC, Boll DT, Paulson EK, Ho LM, Neville AM, et al. Dual-energy multidetector CT: how does it work, what can it tell us, and when can we use it in abdominopelvic imaging? *Radiographics* 2010;30:1037-1055
20. Kis BJ, Sarnyai Z, Kákonyi R, Erdélyi M, Szabó G. Single-energy material decomposition using X-ray path length estimation. *J Comput Assist Tomogr* 2012;36:768-777
21. Siddon RL. Fast calculation of the exact radiological path for a three-dimensional CT array. *Med Phys* 1985;12:252-255
22. Ingle Jr JD, Crouch SR. Spectrochemical analysis. *Englewood Cliffs: Prentice Hall* 1988:590
23. Johnson T, Fink C, Schönberg SO, Reiser MF. *Dual energy CT in clinical practice.* Berlin, Heidelberg: Springer 2011
24. Brooks RA. A quantitative theory of the Hounsfield unit and its application to dual energy scanning. *J Comput Assist Tomogr* 1977;1:487-493
25. Kalender WA, Klotz E, Kostaridou L. An algorithm for noise suppression in dual energy CT material density images. *IEEE Trans Med Imaging* 1988;7:218-224
26. Warp RJ, Dobbins JT 3rd. Quantitative evaluation of noise reduction strategies in dual-energy imaging. *Med Phys* 2003;30:190-198
27. Feldkamp LA, Davis LC, Kress JW. Practical cone-beam algorithm. *J Opt Soc Am A* 1984;1:612-619
28. Macovski A, Nishimura DG, Doost-Hoseini A, Brody WR. Measurement-dependent filtering: a novel ap-

proach to improved SNR. *IEEE Trans Med Imaging* 1983;2:122-127

29. Nishimura DG, Macovski A, Brody WR. Noise reduction methods for hybrid subtraction. *Med Phys* 1984; 11:259-265

30. McCollough CH, Van Lysel MS, Peppler WW, Mistretta CA. A correlated noise reduction algorithm for dual-energy digital subtraction angiography. *Med Phys* 1989;16:873-880

31. Brenner DJ, Hall EJ. Computed tomography--an increasing source of radiation exposure. *N Engl J Med* 2007;357:2277-2284

32. Mettivier G, Russo P, Cesarelli M, Ospizio R, Passeggio G, Roscilli L, et al. Dedicated scanner for laboratory investigations on cone-beam CT/SPECT imaging of the breast. *Nucl Instrum Methods Phys Res* 2011;629:350-356

33. Crotty DJ, Brady SL, Jackson DC, Toncheva GI, Anderson CE, Yoshizumi TT, et al. Evaluation of the absorbed dose to the breast using radiochromic film in a dedicated CT mammotomography system employing a quasi-monochromatic x-ray beam. *Med Phys* 2011;38:3232-3245

34. Coleman AJ, Sinclair M. A beam-hardening correction using dual-energy computed tomography. *Phys Med Biol* 1985;30:1251-1256

35. Wong CK, Huang HK. Calibration procedure in dual-energy scanning using the basis function technique. *Med Phys* 1983;10:628-635

36. Kachelriess M, Sourbelle K, Kalender WA. Empirical cupping correction: a first-order raw data precorrection for cone-beam computed tomography. *Med Phys* 2006;33:1269-1274

37. Stenner P, Berkus T, Kachelriess M. Empirical dual energy calibration (EDEC) for cone-beam computed tomography. *Med Phys* 2007;34:3630-3641

약하게 조영증강된 병변의 유방 전용 CT 영상의 대조도 개선을 위한 적응적 영상 재조정 방법: 팬텀 연구

김빛별[1] · 김호경[1] · 김진성[2] · 기용간[3] · 주지현[4] · 전호상[4*] · 박 달[5] · 김원택[3] · 남지호[5] · 김동현[5]

목적 Dedicated breast CT (이하 DBCT)는 유방 압박의 고통이 없는 영상 진단 기법으로 최근 주목받고 있다. 본 연구에서는 DBCT 영상에서 약하게 조영증강된 작은 병변의 검출률을 높이기 위해 피사체의 기하학적 정보를 이용하여 최적의 영상 문턱값을 제공하는 adaptive image rescaling (이하 AIR) 기법을 제안하였다.

대상과 방법 5개의 동일 크기의 구멍과 서로 다른 크기의 구멍을 가지는 두 개의 디스크를 각각 제작하고, 이를 60 kVp와 100 kVp로 스캔하여 single-energy CT (이하 SECT), dual-energy CT (이하 DECT), 그리고 AIR 영상을 생성하였다. 전임상 평가를 위해 돼지 조직 영상도 획득하였다. Image contrast (이하 IC)와 contrast-to-noise ratio (이하 CNR)로 화질을 평가하였으며, student's *t* test를 이용하여 영상 간 화질의 차이를 검증하였다.

결과 AIR의 평균 IC (0.70)는 DECT (0.94)의 74.5%로 나타났으며, SECT (0.22) 보다 318.2% 높았다. 또한 AIR의 평균 CNR (5.08)은 SECT (14.30)의 35.5%로 나타났고 DECT (2.28) 보다 222.8% 높게 측정되었다. 돼지 조직의 전임상 평가 결과도 비슷한 양상을 보였다.

결론 AIR은 SECT보다 높은 영상 대조도를 가지며, 50% 선량만으로도 DECT에 비견할 만한 화질 성능을 제공할 수 있음을 확인하였다. 따라서 AIR은 DBCT 영상에서 약하게 조영증강된 병변의 검출률을 개선할 수 있을 것으로 생각된다.

[1]부산대학교 기계공학부,
[2]연세대학교 의과대학 방사선종양학교실,
[3]부산대학교 의과대학 방사선종양학교실,
[4]양산부산대학교병원 방사선종양학과, 의생명융합연구소,
[5]부산대학교병원 방사선종양학과